frontiers | Frontiers in Energy Research

ORIGINAL RESEARCH
published: 25 April 2022
doi: 10.3389/fenrg.2022.839898

Thermal Management and Dynamic Performance of a Cooler Design for the Supercritical CO2 Turbine Shaft Cooling

Jun Li[1], Hal Gurgenci[2], Zhiqiang Guan[2], Jishun Li[1], Yujun Xue[1] and Lun Li[1]*

[1]School of Mechatronics Engineering, Henan University of Science and Technology, Henan Key Laboratory for Machinery Design and Transmission System, Henan University of Science and Technology, Luoyang, China, [2]School of Mechanical and Mining Engineering, University of Queensland, Brisbane, QLD, Australia

This paper presents the results of a numerical study on a supercritical CO2 (SCO2) turboshaft cooling device by considering heat transfer and hydrodynamics. A micro-cooling device with a radius clearance of 50 micron and a nozzle diameter of 4 mm was designed and used to investigate the heat transfer characteristics of a micro-spacing impinging and gas film dynamics. Sixteen nozzles (N = 16) are equally spaced around the shaft in single or double rows. Investigations include journal speed- and eccentricity-dependent forward and cross-coupled force coefficients, and the effects of nozzle layouts and mass flow rate on the heat transfer efficiency. Analysis of the correlation coefficient shows that the gas density in the radial clearance is the dominant factor affecting the convective heat transfer performance, while the fluid velocity is a secondary factor. And the cooling efficiency (mass flow utilization rate) at low cooling pressure (p_s < 0.7 MPa) is significantly greater than that at high cooling pressure (p_s > 0.7 MP). In addition, considering the structure alone, a dual-row cooler exhibits a higher average Nusselt number, also registers a higher mass flow rate at the same pressure. Once the shaft is heated only one end, the difference in effectiveness between single- and dual-row cooling is not significant, so coolers with a single-row configuration should be preferred. Then, experimental values for the temperature of the heated rotor are provided under specific cooling airflow conditions. Dynamic analysis results show that the force coefficient of the single-row configuration is more dependent on the journal rotation speed and eccentricity ratio, and exhibits a negative direct stiffness coefficient at higher inlet pressure and journal rotation speed. Moreover, cross-coupled terms (stiffness coefficient) generally have a more explicit variation tendency than direct terms, and are more sensitive to changes in shaft speed and eccentricity. Small clearance cooling is a relatively complex technology aimed to improve heat dissipation efficiency in gas cooling devices while minimizing the effect of hydrodynamic pressure. Comparing the gas force coefficients of different journal speeds reveals a drastic increase in the effect of hydrodynamic pressure when the journal is eccentric. The cooler may be considered for operation with compliant support (such as bump foil) to generate additional damping and appropriately compensate for the eccentricity of the rotor.

Keywords: shaft cooling, gas film stiffness, heat transfer, cooler, jet impingement

OPEN ACCESS

Edited by:
Mostafa S. Shadloo,
Institut national des sciences appliquées de Rouen, France

Reviewed by:
Fubin Yang,
Beijing University of Technology, China
Jie Gao,
Harbin Engineering University, China

****Correspondence:***
Jishun Li
li_jishun@163.com

Specialty section:
This article was submitted to Process and Energy Systems Engineering, a section of the journal Frontiers in Energy Research

Received: *20 December 2021*
Accepted: *14 March 2022*
Published: *25 April 2022*

Citation:
Li J, Gurgenci H, Guan Z, Li J, Xue Y and Li L (2022) Thermal Management and Dynamic Performance of a Cooler Design for the Supercritical CO2 Turbine Shaft Cooling. Front. Energy Res. 10:839898. doi: 10.3389/fenrg.2022.839898

INTRODUCTION

The supercritical carbon dioxide (SCO2) cycle has attracted widespread attention owing to its enhanced efficiency at higher turbine inlet temperatures, and its effective utilization in various next generation power plants, such as nuclear, fossil fuel, waste heat, and renewable heat sources (Turchi et al., 2013; San Andres et al., 2011a; Ahmadi et al., 2018; White et al., 2021; Ahn et al., 2015). Numerical (Alawadhi et al., 2021; Khatoon et al., 2021), experimental (Marchionni et al., 2021; Arslan and Guzel, 2021), and theoretical (Lee et al., 2021; Persico et al., 2021) investigations have probed into various fundamentals as well as practical applications of SCO2 Brayton cycles. Multiple factors make SCO2 a preferred circulating medium for next generation of power conversion systems including smaller heat exchangers, simple physical layouts, reliability and safety with conventional structure materials, compact turbomachinery and high efficiency at the higher turbine inlet temperatures (500–900°C) (Pandey et al., 2020; Penkuhn and Tsatsaronis, 2020). It is generally accepted that regions with relatively high turbine inlet temperatures perform much better than regions with lower temperatures. However, due to the high temperature, compatibility issues inevitably arise for the design of bearings and seals in SCO2 Brayton cycle turbomachinerys.

The supercritical CO2 turbine configuration adopted by the Australian Solar Thermal Research Institute (ASTRI) is a radial turbine where the rotor is mounted at the end of an overhung shaft (**Figure 1**). In order to meet the conventional bearings and dry gas seals requirement on temperature, a cooling zone is provided between the impeller on the cantilever and the dry gas seal. The cooler proposed in this paper aims to protect the dry gas seals and the bearings inside the gearbox against the high temperatures at the turbine exhaust.

Besides of the thermal management for the dry gas seal and the bearings, the paper will also propose the use of a "cooling device" to add extra stiffness to support the rotor of the turbine. By "Cooling device", it means a high-clearance journal bearings with cool CO2 flowing through the annulus passage to cool the shaft. The cooler is not a true journal bearing. Its clearance is selected to provide adequate cooling. The flow in the annular passage in the cooling device will be simulated using computational fluid dynamics (CFD). The cooling device stiffness and damping values (as predicted in CFD) are combined with the shaft model of SCO2 turbine. The results will give the predicted critical speed and damping for the SCO2 turbine. Before that, the convective heat transfer characteristics of the cooling device should be studied in detail. The unbalanced response of the turbine impeller and the cooling efficiency of the cooler are being influenced by the impingement separation distance of nozzle and shaft surface, and the velocity in the radius clearance (**Figure 1**) is affected by the conversion of pressure gradient with the momentum. In addition, the flow structure is more intricate as the jet impingement are impacted by adjacent wall jets and micro scales limiting the average velocity of the fluid (Adeoye et al., 2021).

The reasons for instability in hot turbines, in addition to unbalanced mass on the cantilever, may be a resonance, misalignment and a too high shaft temperature. A very important issue is the thermal creep and uneven thermal expansion of the structural components during hot turbine operation. To control temperature gradient of the gas foil bearings, Lubieniecki et al., 2016 and Martowicz et al. (2020) proposed a method of thermoelectric coolers. With a traditional but effective approach, Ryu (2012) implemented a thermal management in gas foil bearings system which is to supply pressurized air inside the bearing to control thermal growth of foils. A similar case, San Andres et al. (2011b) presented full details on the test data and analytical results for dynamic and thermal performance of gas foil bearings system with a cooling gas stream condition.

Most of the previous numerical and experimental studies have reported a high heat transfer coefficient in the jet impingement cooling region, which have been used in various industrial applications (GhadikolaeiAlotaibi et al., 2020; 2021; Maghrabie, 2021; Modak et al., 2021). Several studies have also explored micro-scale impinging jets and reported a significantly different heat transfer characteristics compared to the results obtained at the normal scale. Lau et al. (2021) reported an enhanced overall cooling performance for a water jet with Al2O3 nano-fluid in their study of heat transfer enhancement on a microchannel single synthetic jet impinging. Adeoye et al. (2021) experimentally studied micro-nozzle (206 μm) impingement on a thick fused silica substrate with supercritical carbon dioxide and noted the differences between available correlations and experiments. Patil and Narayanan (2005) compared experimental average Nusselt numbers (Nu_{av}) of microscale circular nozzle (nozzle diameter d_i = 125 μm) jet impingement to the earlier investigation of Martin and noted that there were notable deviations for the both low Reynolds numbers (Re) and high Re normal scale jet impingement. A numerical study by Li et al. (2021) reported significant enhancements of the heat transfer for CO2 jet impinging when the separation distance between nozzle and target surface was reduced from 0.1 to 0.05 mm. However, it is rare to study the heat transfer performance of gas films in the radial clearance between rotating shaft and cooler.

A previous study (Kim et al. (2019) has shown that a single-phase hybrid micro array jet impingement can attain strong impingement effects caused by reduced diameter of jet nozzles. However, the nozzle-to-surface spacing is still mainly responsible for the heat transfer efficiency for a given mass flow rate (Ahmed et al., 2021). Although this conclusion demonstrates the high performance of hybrid micro-scales with water for cooling, its compatibility with gas cooler of rotor systems remains a concern. For the SCO2 turbine rotor shaft cooling, the multi-nozzle is employed in the pattern of a row or array jets evenly distributed around the shaft (**Figure 1**). For this reason, gaseous refrigerant, such as supercritical carbon dioxide in the Brayton cycle has been taken into consideration, but because of the high pressure (the CO2 critical condition is 30.98°C and 7.38 MPa), dynamic characteristics of the jets especially need to be investigated. The overall heat transfer of shaft surfaces increases by creating very small clearance which also limits the expansion of the gas near the heat transfer surface. The main reason is that using high

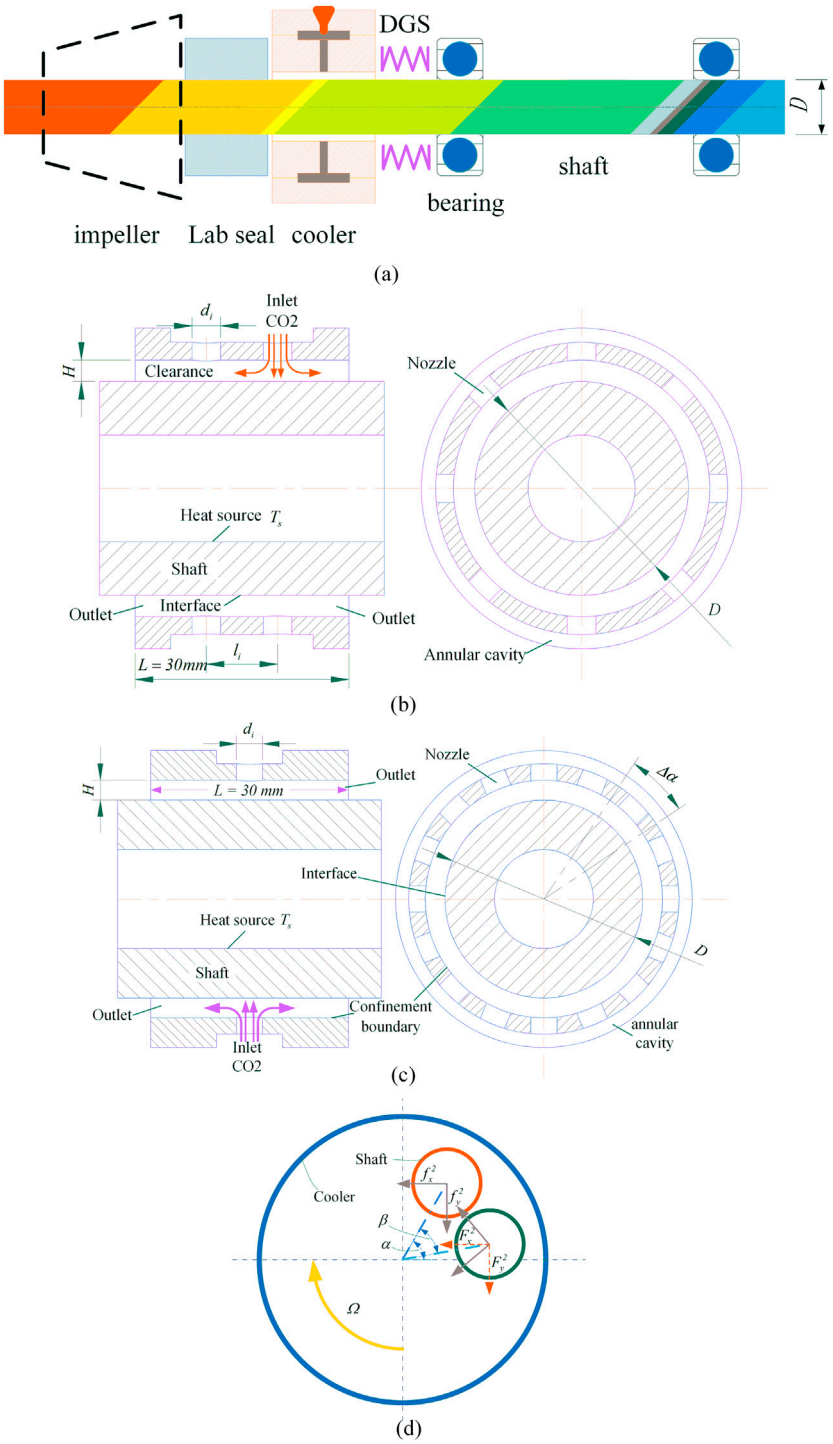

FIGURE 1 | Working mechanism of the proposed cooler and shafting for SCO2 turbine. **(A)** Schematic diagram of bearing-rotor system. **(B)** double row. **(C)** single row. **(D)** Schematic graph of rotating frame with cooler describing a journal with amplitude *e* and attitude angle α. Stationary coordinate (*X, Y*) and its rotation angle β are noted.

pressure CO2 in a very small clearance for heat transfer augmentation typically incurs a strong dynamic pressure effect, which causes potential instabilities of the high speed rotor system. To alleviate this issue, the stiffness and damping of the gas film are also the topics that have to be carefully examined and designed.

Experimental and numerical investigations have been carried out on several different configurations to study the dynamic

TABLE 1 | Boundary conditions and parameter values for the numerical studies.

Parameters	Range
Outlet pressure p_o (*MPa*)	0.1
Inlet pressure p_s (*MPa*)	0.2–2.0
Inlet temperature T_{CO2} (*K*)	330
Heat source T_s (*K*)	1,073
Rotor speed *n* (*rpm*)	0–50,000
nozzle diameter d_i (mm)	4
nozzle to rotor surface spacing *H* (mm)	0.05
Length of cooler *L* (mm)	30
Diameter of the shaft *D* (mm)	30
Number of nozzles N_i	16 (single or double row)

TABLE 2 | Correlation coefficients between the average Nusselt number and the variables analyzed.

Correlation Coefficient	Parameters	Double Row	Single Row
$R_{XY} = \frac{\sigma_{XY}}{\sqrt{\sigma_{XX}}\sqrt{\sigma_{YY}}}$	$X = Nu_{av}$ $Y = \rho_{av}$	R_{XY} = 0.998	R_{XY} = 0.9974
	$X = Nu_{av}$ $Y = v_{av}$	R_{XY} = 0.5934	R_{XY} = 0.2935

performance of gas film, such as gas foil bearings (Basumatary et al., 2020; Zhang et al., 2018; Zywica et al., 2021), self-acting gas journal bearings (Feng et al., 2017; Zhang et al., 2014), and other externally pressurized gas bearing (Moore et al., 2011; Han et al., 2014; Ise et al., 2014). Although the pressure distribution of the gas film obtained numerically with standard Reynolds equation is approximately to determine the stiffness and damping, the thermally coupled analysis of the bearing may be impeded. In the model of the cooler, the radius clearance (50 μm) is large enough to maintain sufficient flow while attenuating the dynamic pressure effect. Although the assumption of the Reynolds equation for the gas film of the bearing is reasonable, it is obviously no longer applicable for the gas jet impingement with a slightly larger gap. A 3D mesh with radial boundary layers is necessary. This paper, employing the commercial computational tool Fluent, presents extensive predictions of the temperature field and dynamic force coefficients, as well as various other parameters, of a 3D model of the rotor cooler.

To sum up, a reliable implementation of conventional bearings (such as gas foil bearings, angular contact ball bearings and oil film bearings) and seals into high temperature SCO2 turbomachinery requires effective thermal management to maintain rotor system stability. Another purpose of this paper is to tailor the cooler stiffness in both forward and cross directions, thereby minimizing the dynamic pressure effect of gas film, to maintain a reasonable compliance and accommodate mechanical distortions as well as misalignment of the shafts. The cooler proposed in this paper is inspired by the external gas bearing and jet impingement, as the coolant is a high-pressure CO2 gas, with the impinging jet is normal to the surface of the shaft. There are constrains on the radius clearance between the shaft surface and the nozzle mounting surface (confinement surface) to provide additional throttling effect for the cooling device and improve the cooling efficiency of the airflow.

THE PHYSICAL PROBLEM AND METHOD OF ANALYSIS

Computational Fluid Dynamic Modeling and Boundary Conditions

The cooler consists of 16 nozzles assembly oriented normal to the rotor shaft surface. The geometry of the fluent model is symmetry with the axis as shown in **Figure 1**. However the circumferential symmetry only happens when the shaft is at the geometric center of the cooler, dynamic pressure effect of gas film is inevitably caused by the rotating speed and displacement of the shaft. The dynamic pressure effect of minimum gas film thickness between shaft surface and the bearing inner surface provides cross force may well in excess of forward force obtained around the nozzle. The symmetry of the gas film dynamics no longer exists. And, the negative cross-acting force promotes the whirl of the rotor is also one of the important factors of system instability. Hence, full of the inlet, nozzles, clearance are modeled as real CO2 gas fluids in commercial CFD software, and shaft is modeled as steel solid. The hollow shaft is the superficial heat generating source and the constant amount of temperature is 1073 K in core. Inlet of nozzles is the momentum source of jets which is set as a pressure inlet or mass flow rate conditions. The outlet boundary condition is set to a pressure of 0.1 MPa. An isothermal no-slip boundary condition was assumed with the rotor surface and adiabatic condition for the other walls. With the purpose of getting a comprehensive investigation for the stiffness, damping and heat transfer efficiency in the micro-clearance jet impingement, the CFD software Fluent 19.1 and computer cluster have been utilized. The nozzle rows, the jet-to-surface spacing and rotation speed of shaft are variable to assess how they have impacts on heat transfer rate and kinetic characteristics of gas film. Several different combinations of boundary conditions and nozzle configurations were considered as summarized in **Tables 1** and **2**.

Governing Equation

As a conclusion of the previous experimental and numerical preliminary investigation, that the ideal turbulence model does not exist, as is commonly asserted in a jet impingement analysis (Ehsan et al., 2019).As a compromise, many investigations have concluded that Reynolds-averaged *k-omega* turbulence model shows reasonably admissible performance in gas jet impact prediction (Lapka et al., 2020; Tepe, 2021; Tepea et al., 2020). Considering the complex flow of jet impact and the high-speed rotation of the shaft, the flow in the computational domain was depicted by the *k-omega* model (Lapka et al., 2020). The governing equations in the computation are the Reynolds-averaged mass, momentum, and energy. The equations with steady-state compressible fluid properties are expressed as:

Continuity Equation:

$$\begin{cases} \frac{\partial}{\partial x_i}(\rho u_i) = 0 \\ \frac{\partial}{\partial x_j}(\rho u_i u_j) = -\frac{\partial p}{\partial x_i} + \frac{\partial}{\partial x_j}\left[\mu\left(\frac{\partial u_i}{\partial x_j} + \frac{\partial u_j}{\partial x_i} - \frac{2}{3}\delta_{ij}\frac{\partial u_i}{\partial x_i}\right)\right] + \frac{\partial}{\partial x_j}\left(-\rho\overline{u_i' u_j'}\right) \end{cases} \quad (1)$$

Momentum Equation:

$$\frac{\partial(\rho u_i u_j)}{\partial x_j} = -\frac{\partial p}{\partial x_i} + \frac{\partial}{\partial x_j}\left[\mu\left(\frac{\partial u_i}{\partial x_j} + \frac{\partial u_j}{\partial x_i} - \frac{2}{3}\delta_{ij}\frac{\partial u_i}{\partial x_j}\right)\right] + \frac{\partial}{\partial x_j}\left(-\rho\overline{u'_i u'_j}\right) \tag{2}$$

Where, $-\rho\overline{u'_i u'_j}$ is Reynolds stress denotes the effect of turbulence (Tepea et al., 2020), u is the velocity, u' is the turbulent velocity, p is the pressure, μ is the dynamic viscosity, ρ is the density.

Energy Equation:

$$\frac{\partial}{\partial x_j}\left[\mu_i(\rho E + p)\right] = \frac{\partial}{\partial x_j}\left[\left(\kappa_e + \frac{c_p \mu_i}{Pr_t}\right)\frac{\partial T}{\partial x_j} + \mu_i\left(\tau_{ij}\right)_e\right] \tag{3}$$

Where, i, j, k = 1, 2, 3 are indices of Cartesian axes, c_p is the specific heat, T is the temperature, κ_e is the effective thermal conductivity, and Pr_t is the turbulent Prandtl number, E is total energy, $(\tau_{ij})_e$ is the deviatoric stress tensor (Marzec, 2020). The above equations will be closed by the SST $k-\omega$ model. The standard $k-\omega$ model has the characteristics of near-wall stability and sensitivity to adverse pressure gradient. The $k-\varepsilon$ model has the advantage of independence from the boundary layer. Menter (1994) introduced hybrid functions to combine the two modes into one, and developed $k-\omega$ into the shear stress transport model (SST $k-\omega$). The improved model is more accurate and reliable over a wide range of flows than its standard form. Refer to the paper for a detailed introduction of the SST k-w model.

The Reynolds number of nozzles is defined as follows:

$$Re = \frac{\rho v d_i}{\mu} = \frac{4q}{\pi N_i d_i \mu} \tag{4}$$

Where, ρ is the CO2 fluid density, kg/m^3; v is the average velocity at the inlet of nozzles, m/s; d_i is the nozzle diameter, m; and μ is dynamic viscosity, $Pa \cdot s$; q mass flow rate, kg/s; N_i is number of nozzles. For lubrication flow and eccentric annular rings, the Reynolds number is expressed as

$$Re = \frac{\rho u L}{\mu}\left(\frac{c}{L}\right)^2 \tag{5}$$

Where u = 78.54m/s is the rotor working speed and $L = 30mm$ is the width of the hydrostatic zones. Here, constant fluid temperature at the extreme case are represented by $T = 330\,K$. The Re in **Eq. 5** are depicted in terms of the lines with symbols in **Figure 2A**. These data represent the turbulence intensity (I) and can be used as a reference for setting boundary conditions. The I determined by

$$I = 0.16Re^{-1/8}$$

The dimensionless convective heat transfer rates along the cooled rotor surface are defined in terms of the Nusselt number, and the local Nu_l can be calculated as:

$$Nu_l = \frac{h_l D}{k_c} \tag{6}$$

Averaged Nu number can be determined as:

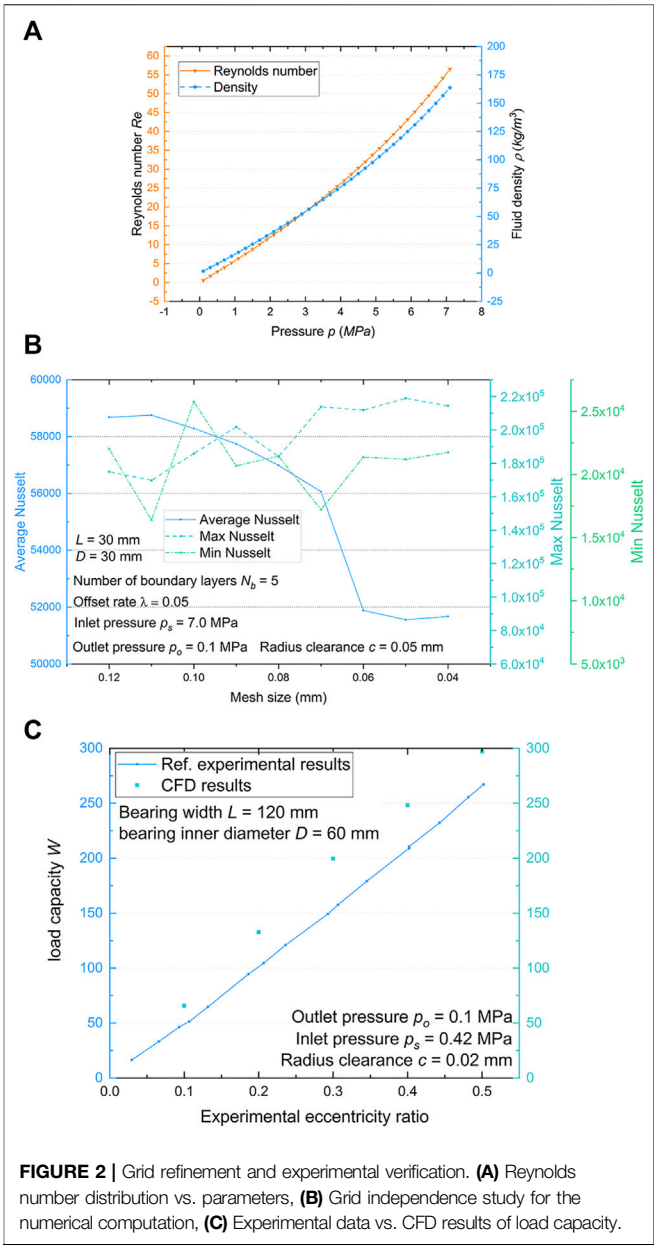

FIGURE 2 | Grid refinement and experimental verification. **(A)** Reynolds number distribution vs. parameters, **(B)** Grid independence study for the numerical computation, **(C)** Experimental data vs. CFD results of load capacity.

$$Nu_{av} = \frac{h_{av} D}{k_c} \tag{7}$$

Where, k_c represents the thermal conductivity of the fluid material. The term h is the local heat transfer coefficient obtained by numerical computation (Fp et al., 2010). The average heat transfer coefficient is defined as

$$h_{av} = \frac{1}{A}\int_A h_l dA \tag{8}$$

Analysis of Gas Film Forced Performance

The wall boundary conditions for the gas film are the stationary wall and the rotating surface on the inner wall of the bearing and the surface of the shaft, respectively. In the case of gas bearing,

dynamic gas forces are calculated based on the shaft eccentricity and whirling velocity perturbations. It can be defined as the following:

$$\begin{bmatrix} F_x \\ F_y \end{bmatrix} = \begin{bmatrix} F_x^0 \\ F_y^0 \end{bmatrix} + \begin{bmatrix} k_{xx} & k_{xy} \\ k_{yx} & k_{yy} \end{bmatrix} \cdot \begin{bmatrix} \Delta e_x \\ \Delta e_y \end{bmatrix} + \begin{bmatrix} c_{xx} & c_{xy} \\ c_{yx} & c_{yy} \end{bmatrix} \cdot \begin{bmatrix} \left(e_y^0 + \Delta e_y\right)\Delta\Omega \\ \left(e_x^0 + \Delta e_x\right)\Delta\Omega \end{bmatrix} \tag{9}$$

Where, F_x^0 and F_y^0 are the gas film forces without disturbance, k_{ij} and c_{ij} represent the stiffness and damping at a given rotational speed and eccentricity, respectively. $\Delta\Omega$ is the whirl frequency perturbation of the shaft. The small constants $[\,\Delta e_x^0 \quad 0\,]^T$ and $[\,0 \quad \Delta e_y^0\,]^T$ are the perturbed displacements at rotational frequency ω_0 and whirl frequency Ω_0 of the shaft. The new film forces, at displacement $(e_x^0 + \Delta e_x)$ and $(e_y^0 + \Delta e_y)$, is assumed to vary linearly with whirl frequency perturbation as $[\,f_x^{12} \quad f_y^{12}\,]^T$ and $[\,f_x^{11} \quad f_y^{11}\,]^T$.

Accordingly, the damping and stiffness in the thin film is assumed to behave as linear changes at the occurrence of minor perturbations, and hence the equation of followings (**Eqs. 10–19**) are used to express the kinetic characteristics of gas film as a function of shaft's displacement and whirling velocity disturbances. Damping can be expressed separately as

$$c_{xx} = \frac{f_x^{11} - f_x^{01}}{\left(e_y^0 + \Delta e_y\right)\Delta\Omega} \tag{10}$$

$$c_{xy} = \frac{f_x^{12} - f_x^{02}}{\left(e_x^0 + \Delta e_x\right)\Delta\Omega} \tag{11}$$

$$c_{yy} = \frac{f_y^{12} - f_y^{02}}{\left(e_x^0 + \Delta e_x\right)\Delta\Omega} \tag{12}$$

$$c_{yx} = \frac{f_y^{11} - f_y^{01}}{\left(e_y^0 + \Delta e_y\right)\Delta\Omega} \tag{13}$$

Where, $[\,f_x^{01} \quad f_y^{01}\,]$ and $[\,f_x^{02} \quad f_y^{02}\,]$ are obtained when the steady state position of the rotor is perturbed by small translational displacements $[\,\Delta e_x^0 \quad 0\,]^T$ and $[\,0 \quad \Delta e_y^0\,]^T$. Gas film stiffness and damping calculation is a nonlinear problem in which the eccentricity must be considered case-by-case. Therefore, in the present study, the radius clearance is discretized with an interval of 5 microns and the perturbation method is used to linearize the variation of stiffness and damping. The linearized equations are then expressed iteratively as

$$\begin{bmatrix} f_x^{21} \\ f_y^{21} \end{bmatrix} = \begin{bmatrix} f_x^0 \\ f_y^0 \end{bmatrix} + \begin{bmatrix} k_{xx} & k_{xy} \\ k_{yx} & k_{yy} \end{bmatrix} \cdot \begin{bmatrix} \Delta e_x \\ \Delta e_y \end{bmatrix} + \begin{bmatrix} c_{xx} & c_{xy} \\ c_{yx} & c_{yy} \end{bmatrix} \cdot \begin{bmatrix} \Delta e_y\,(\Omega_0 + \Delta\Omega) \\ \Delta e_x\,(\Omega_0 + \Delta\Omega) \end{bmatrix} \tag{14}$$

$$\begin{bmatrix} f_x^{22} \\ f_y^{22} \end{bmatrix} = \begin{bmatrix} f_x^0 \\ f_y^0 \end{bmatrix} + \begin{bmatrix} k_{xx} & k_{xy} \\ k_{yx} & k_{yy} \end{bmatrix} \cdot \begin{bmatrix} \Delta e_x \\ \Delta e_y \end{bmatrix} + \begin{bmatrix} c_{xx} & c_{xy} \\ c_{yx} & c_{yy} \end{bmatrix} \cdot \begin{bmatrix} \Delta e_y\,(\Omega_0 + \Delta\Omega) \\ \Delta e_x\,(\Omega_0 + \Delta\Omega) \end{bmatrix} \tag{15}$$

Hence, the stiffness coefficients, at eccentricity $[\,e_x^0, e_y^0\,]$, are calculated as

$$k_{xx} = \frac{f_x^{21} - f_x^0 - c_{xy}\,(\Delta e_x \Omega_0)}{\Delta e_x}\,, \left(\Delta e_y = 0, \Delta\Omega = 0\right) \tag{16}$$

$$k_{yx} = \frac{f_y^{21} - f_y^0 - c_{yy}\,(\Delta e_x \Omega_0)}{\Delta e_x}\,, \left(\Delta e_y = 0, \Delta\Omega = 0\right) \tag{17}$$

$$k_{xy} = \frac{f_x^{22} - f_x^0 - c_{xx}\left(\Delta e_y \Omega_0\right)}{\Delta e_y}\,, \left(\Delta e_x = 0, \Delta\Omega = 0\right) \tag{18}$$

$$k_{yy} = \frac{f_y^{22} - f_y^0 - c_{yx}\left(\Delta e_y \Omega_0\right)}{\Delta e_y}\,, \left(\Delta e_x = 0, \Delta\Omega = 0\right) \tag{19}$$

Where, f_x^0 and f_y^0 are the gas film forces at eccentricity $[e_x^0, e_y^0]$ of shaft.

In order to introduce a variable whirl frequency, the components of rotor rotational velocity must be coupled to the translational velocity, and the coupled motion is solved for the boundary condition of the shaft surface after considering the displacement disturbance. The translational velocities over each steady state position is determined by the whirl frequency as

$$u_{wx} = \Omega e_y \tag{20}$$

$$u_{wy} = \Omega e_x \tag{21}$$

For a rotating journal operation, the surface gas flow circumferential velocities vary along the Cartesian coordinate x and y as

$$u_{rx} = \omega r \cdot sin(\theta) \tag{22}$$

$$u_{ry} = \omega r \cdot cos(\theta) \tag{23}$$

Where, ω is angular velocity of the rotor rotation, θ is the azimuth in the X-Y plane and r is radius of shaft. The u is the absolute velocity of the airflow on the rotor surface, hereby taken as shaft surface velocity since in the SST *k-omega* model the non-slip boundary condition is adopted. Once the rotational velocities distribution and the translational velocities are obtained, the absolute velocities of the shaft surface can be evaluated as follows:

$$u_x = u_{rx} + u_{wx} \tag{24}$$

$$u_y = u_{ry} + u_{wy} \tag{25}$$

The coupled velocities u_x and u_y are then used as the boundary conditions to calculate the pressure perturbations of the shaft surface which are integrated to carry out the predictions of the dynamic force coefficients.

The number of modeling and the amount of numerical calculation were reduced by application of the rotating coordinate system (RCS) in the calculation of the stiffness coefficient. This section further details RCS methods for predicting stiffness coefficients from dynamic load. The prediction restricts its attention to cylindrical bearings.

Figure 1D depicts a schematic diagram of an extruded gas film with a journal describing a whirl motion with amplitudes e_x and e_y. This diagram involves two coordinate systems, one stationary (X, Y) and one rotation (x, y), with angle (β). $\alpha = 0$ coincides with the X axis, whereas the angular origin of the rotation coordinate is

located on the x axis. The relationship between rotation and stationary frames is to rotate (X, Y) by the angle β to obtain (x, y).

In a CFD analysis, the shaft journal kinematics $[e^0, \alpha]^T$ squeezes the gas film and produces forces f_x^0 and f_y^0 governed by the dynamic pressure and inlet pressure field.

In the rotation coordinate (x, y), the deflection angle of the journal becomes $(\alpha + \beta)$. Whereas, in absolute frame, the journal's displacements equal

$$e = \begin{bmatrix} e_x \\ e_y \end{bmatrix} = \begin{bmatrix} e_x^0 + \Delta e_x \cos(\beta) & e_y^0 + \Delta e_x \sin(\beta) \\ e_x^0 + \Delta e_y \sin(\beta) & e_y^0 + \Delta e_x \cos(\beta) \end{bmatrix} \tag{26}$$

Then the relative displacement is $[\Delta e_x \cos(\beta)\ \Delta e_x \sin(\beta)]$ and $[\Delta e_y \sin(\beta)\ \Delta e_x \cos(\beta)]$. The gas film force on the journal can be determined as

$$k_{xx}\Delta e_x \cos(\beta) + k_{xy}\Delta e_x \sin(\beta) + f_x^0 \cos(\beta) + f_y^0 \sin(\beta) = f_x^{21} \cos(\beta) + f_y^{21} \sin(\beta) = F_x^{21} \tag{27}$$

$$k_{yx}\Delta e_x \cos(\beta) + k_{yy}\Delta e_x \sin(\beta) + f_x^0 \sin(\beta) + f_y^0 \cos(\beta) = f_x^{21} \sin(\beta) + f_y^{21} \cos(\beta) = F_y^{21} \tag{28}$$

$$k_{xx}\Delta e_y \sin(\beta) + k_{xy}\Delta e_y \cos(\beta) + f_x^0 \cos(\beta) + f_y^0 \sin(\beta) = f_x^{22} \cos(\beta) + f_y^{22} \sin(\beta) = F_x^{22} \tag{29}$$

$$k_{yx}\Delta e_y \sin(\beta) + k_{yy}\Delta e_y \cos(\beta) + f_x^0 \sin(\beta) + f_y^0 \cos(\beta) = f_x^{22} \sin(\beta) + f_y^{22} \cos(\beta) = F_y^{22} \tag{30}$$

The dynamic equilibrium relations above reveal that the gas film thickness and its forces are angle-invariant in the rotating coordinate system. However, the estimation above is true only in a cooler configuration neglect of its anisotropy. The inlet gas flow distort the distribution of pressure; consequently, resultant force is no longer invariant in the rotating coordinate system. In other words, the periodicity of the cooler configuration does not exist at arbitrarily small Interval angles.

Grid Refinement and Experimental Verification

The grid independence examinations have been carried out to validate that the results are independent of the mesh element size. Nine grids with degressive element sizes of 0.12, 0.11, 0.1, 0.09, 0.08, 0.07, 0.06, 0.05 and 0.04 mm have been used to examine the mesh resolution independency. Average, maximum and Minimum Nusselt number Nu on target surface at radius clearance H = 0.05 mm, nozzle diameter d_i = 4 mm, rotor speed n = 60,000 rpm and extreme boundary conditions of $\Delta p = 6.9\,MPa$ (mass flow rate $q = 0.112\,kg/s$) were investigated for the validation. The convergence procedures of the predicted average Nusselt number on the surface with mesh refinement are shown in **Figure 2B**. It can be noticed that deviation of the Nusselt number is less than 1% for the 0.05 mm, 0.04 mm grids. Consequently, the element size of 0.05 mm has been adopted for the purposes of accuracy and saving the iteration time. The radial dimension of the first grid layer adjacent to the shaft surface is set to be 2.5 μm with layers of 5 to ensure that the ceiling amount of local Y-plus is less than 1.0. For this investigation, since the computations were implemented with SST *k-omega* turbulence model, the near wall functions are automatically selected according to the wall-function meshes on the target surface, and the wall treatment is automatically switched between the viscous sublayer formulation and the wall function, depending on the meshing grid refinement (Afroz and Sharif, 2020).

Since the micro-clearance jet impingement is a design similar to the external pressure gas bearing, there is a comparison in the published experimental data for the gas film dynamic characteristics of gas film. The externally pressurized gas bearing referred to in this verification is a rectangular slot restriction type. The actual dimensions and structure of this bearing are same as (Ise et al., 2014). The gas bearing load capacities were evaluated using the results of CFD (in this study) and test data. A symmetrical pressure region admission type journal bearing was used for the sample. The detailed bearing forced performance have been tested and solved numerically in the previous study, where the Reynolds equation was applied to describe the dynamic characteristics of the gas film. The solid line in **Figure 2C** shows the test results of the load capacity of the gas bearing relative to the eccentricity ratio for dimensionless inlet pressure P_s = 4.2. Eccentricity ratio ε is defined by e/c. Where e is rotor displacement from bearing geometric center, c is the radius clearance. The square dots in **Figure 2C** shows the CFD results vs. eccentricity ratio. These boundary conditions are the same as those used in the previous tests of this type of gas bearing, and all calculations use a real gas model of carbon dioxide. The CFD results are compared with experimental load capacities at the eccentricity ratio of ε = 0.2, 0.4, 0.6, 0.5. It is demonstrated that there are deviations between the experimental data and the CFD results. The maximum, minimum and average prediction errors are 21.65, 10.16 and 17.84%, respectively. The deviation is observed to increase with increasing eccentricity ratio, but it is still within an acceptable range. In actual calculations, it is found that the stronger the dynamic pressure effect, the stricter the boundary layer mesh requirements.

RESULTS AND DISCUSSION

Thermal Performance of the Cooling Device

The thermal analysis of the cooling system proposed in the study is carried out based on the assumption that the journal is dynamically stable in the geometric center of the cooling device. The journal diameters and the cooler lengths used in the thermal analyses are both 30 mm (see **Table 1**). Due to the reduced distance between the inlet and outlet for double row cooler, the heat transfer capacity contribution from the mass flow rate increases. While the one with single row (inlet assumed to be located in the middle of the two outlet, see **Figures 1B,C**) has a longer throttling distance. Therefore, the combined effect of the density, velocity, and temperature difference of the fluid in the radial clearance should be

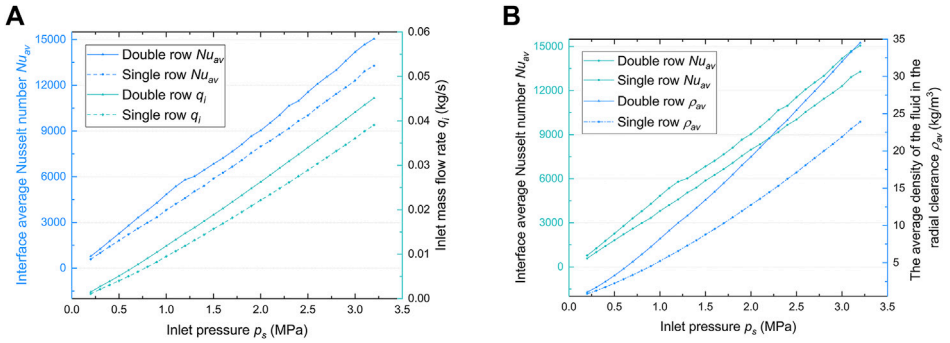

FIGURE 3 | Convection heat transfer performance of dual-row and single-row coolers: **(A)** Interface average Nusselt number Nu_{av} and inlet mass flow rate q_i versus inlet pressure p_s. **(B)** Nu_{av} and Average density of gas in the radius clearance ρ_{av} versus inlet pressure p_s.

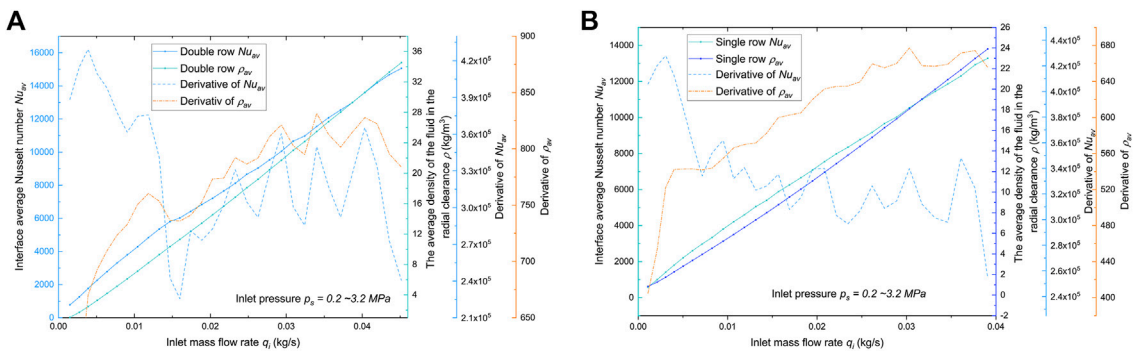

FIGURE 4 | Factors affecting heat transfer efficiency: the average Nusselt number Nu_{av} at the interface, the average density ρ_{av} of the gas in the radius clearance and their derivatives with respect to the mass flow rate q_i, versus q_i. **(A)** Double row, **(B)** Single row.

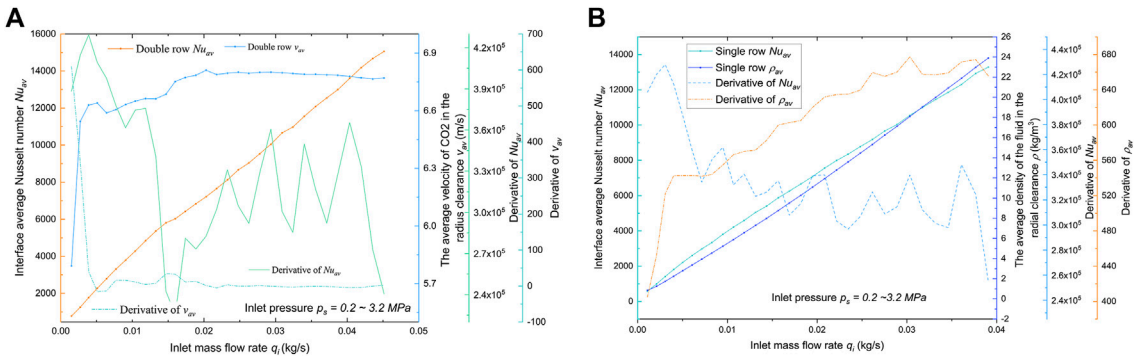

FIGURE 5 | Factors affecting heat transfer efficiency: predicted Nu_{av} at interface, the average velocity v_{av} of the airflow in the radial clearance and their derivatives with respect to mass flow rate q_i, versus q_i. **(A)** Double row, **(B)** Single row.

considered. The Heat transfer performance of gas film is presented in terms of average Nusselt number of the fluid and journal coupling surfaces (**Figure 1**, interface).

Figure 3A compares the pressure-dependent surface-averaged Nusselt distributions. Compared to the single-row configuration, the Nu_{av} in the dual-row configuration showed an average increase of 19.36% at different cooling pressures. Shorter throttling spacing between the nozzle and outlet increases the axial pressure gradient in the radial clearance. Complementarily, the average increase in mass flow rate for the dual-row configuration is 21.53%, which is higher than the Nu_{av} increase in percentage. **Figure 3B** compares the average

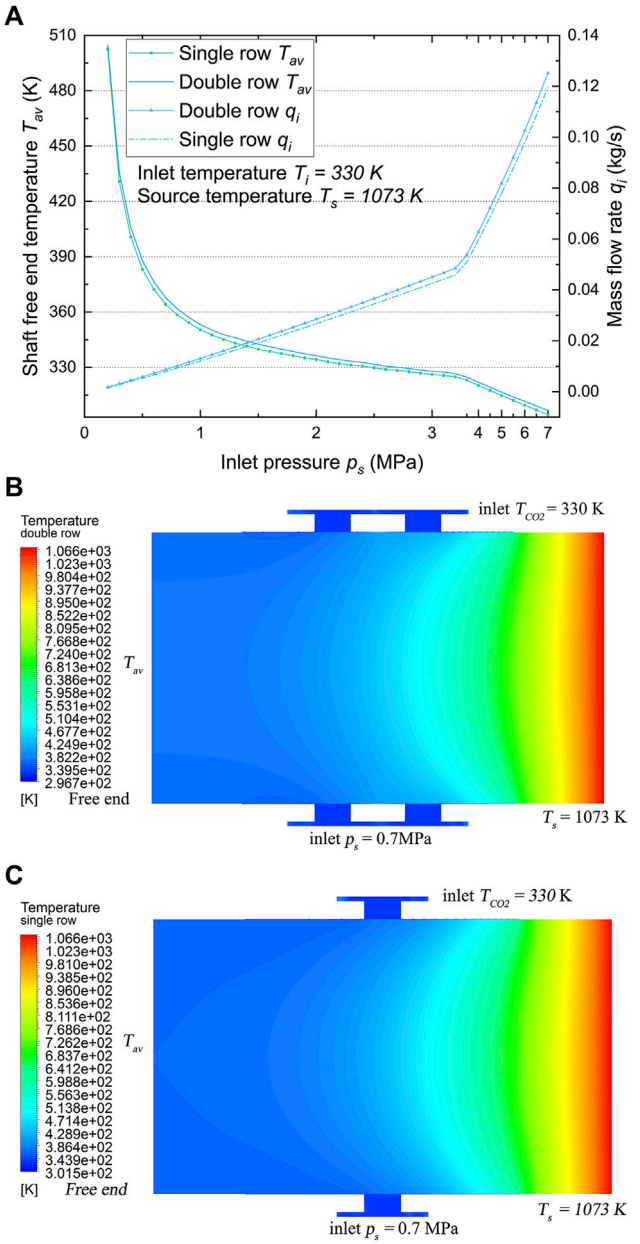

FIGURE 6 | (A) Average temperatures T_{av} at the free end of journal and inlet mass flow rate q_i versus inlet pressure p_s. **(B)** The temperature field of the journal with a double-row inlet cooler. **(C)** The temperature field of the journal with a single-row inlet cooler. The cooling stream temperatures, T_{CO2} = 330 K. The temperature of the heat source, T_s = 1073 K.

density in the radial clearance. The average density of the dual-row configuration is significantly higher than that of the single-row configuration by 49.26%.

The jet gas experiences notable velocity and density variations in the micro-radius clearance. **Figures 4**, **5** presents the averaged Nusselt number Nu_{av}, average density ρ_{av}, average velocity v_{av} and their derivative with respect to mass flow rate for nozzle arrangement of double row and single row. The figures show the derivative of the average density for both double row (case 1) and single row (case 2) respectively, and these derivatives show similar tendency to the cases of derivative of the Nu_{av}. As can be seen, there are significant same variation tendency of derivative of Nu_{av} and derivative of average density, despite the strongly non-linear behavior observed in practical calculations. However, this consistency is significantly lower for the derivative of average velocity presented in the pictures compared to the derivative of ρ_{av}. Further, the correlation coefficient can be used as an indicator to verify these conclusions. The correlation values reported in **Table 2** are calculated using the data in **Figures 8**, **9**. The R_{XY} of the nonlinear correlation metric shows consistent results and a strong positive correlations in evaluating the average density for both double and single rows. The second row of the table data shows the correlation coefficient between the average Nusselt number and the average velocity. Although there are differences in the results for double and single rows, they are all significantly smaller than the R_{XY} between density and Nusselt number. Therefore, these facts suggest that the density of the gas in the radial clearance dominates the convective heat transfer performance.

Further thermal analysis is performed on the solid shaft heated at the right end for the coolers of both configurations. The results of this investigation are shown in **Figure 6**. The average temperature at free end of journal with double row cooler is slightly higher (0.71% on average) due to half the nozzles away from elevated temperature. In addition, the total mass flow rate increased slightly (7.3% on average) over the entire pressure range compared to the single-row configuration. The maximum averaged temperature of free end are around 505 *K* (double row) and 503 *K* (single row) when cooling gas pressure supplied is only 0.2 *MPa*, while increasing the gas pressure to 0.7 *MPa* drops the average temperature significantly to around 368 *K* (double row) and 364 *K* (single row). Steps further on, the average temperature of free end can even be maintained below the temperature of coolant with an extremely high inlet pressure due to expansion of endothermic. However, it is noteworthy that the cooling efficiency of the cooler with low cooling pressure (p_s < 0.7 *MPa*) is significantly larger than the case with high cooling pressure (p_s > 0.7 *MP*). Higher pressure means more energy and gas wasted.

In general, although the mass flow rate and average Nusselt number in cases 1 and 2 do differ significantly, the temperatures T_{av} do not (**Figure 6A**). **Figures 6B,C** shows the cooling system temperature field along the axial direction for both cases with inlet pressure of 0.7 *MPa*. The right end is in thermal contact to the hot impeller (T_s = 1073 *K*) and the left end (free end) is in thermal contact with the bearing unit (considered as adiabatic in this study). Due to the coolant injected into radius clearance flows out along the axial direction (both elevated and low temperature side), the rotor temperature sharply drops. The journal temperature has slightly higher thermal gradient along the axial direction for case with single row nozzles because of more cooling effect at the nozzle and at the location with the larger

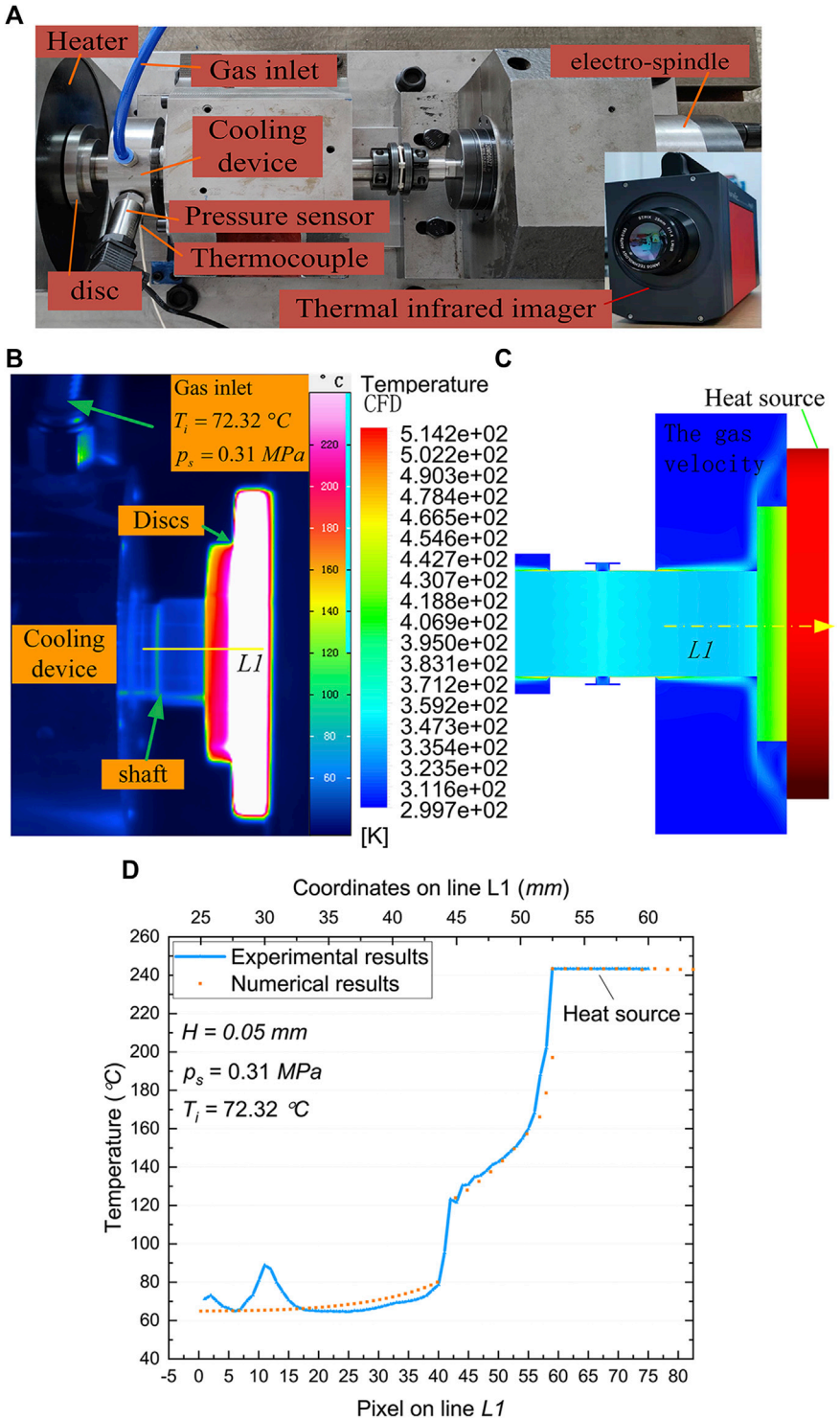

FIGURE 7 | Experimental setup and results. **(A)** Test rig for the measurement of the temperature field of the rotor. **(B)** Experimental results. **(C)** Numerical results. **(D)** Experimental and numerical temperatures on the line L1.

temperature difference. The tendency can also be observed in the shaft temperature field shown in **Figure 6A**. Demonstrated in the figures is the basic principle for impingement heat transmission that a stream impacts directly onto the target surface with thermal boundary layers to transfer heat efficiently.

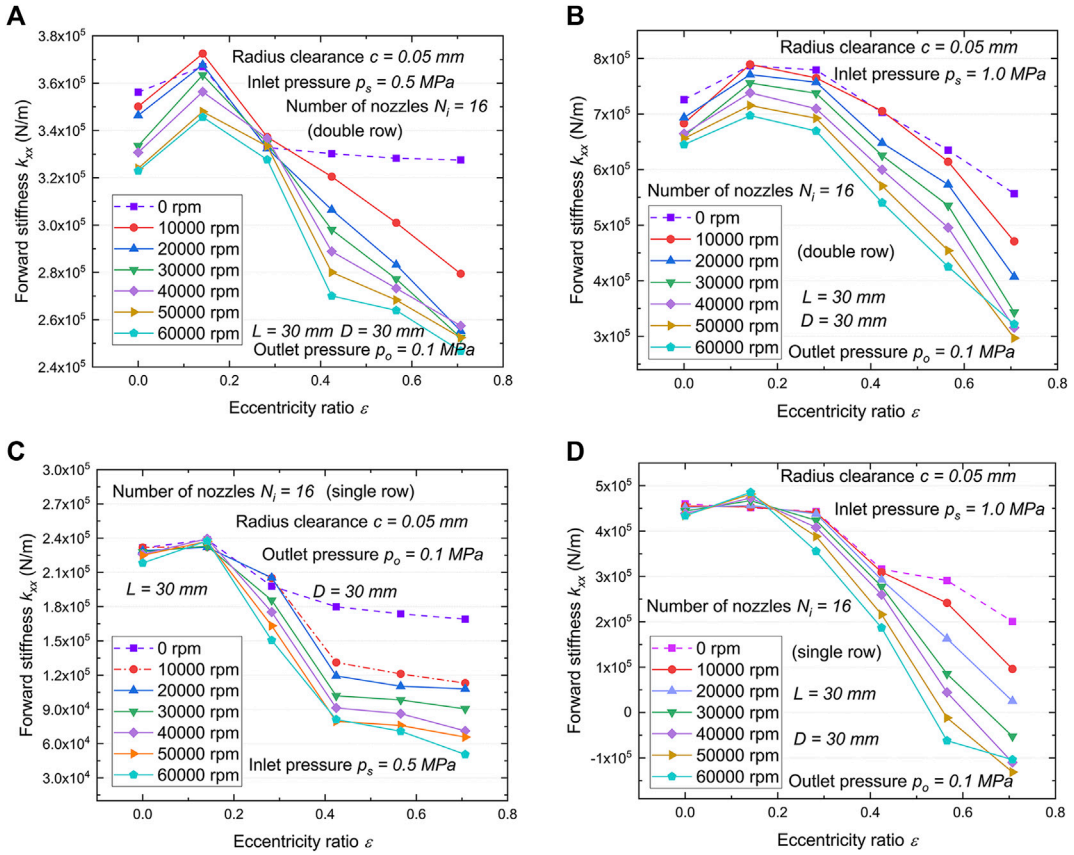

FIGURE 8 | Variations of forward stiffness coefficient k_{xx} with eccentricity ratio. **(A)** Double row, p_s = 0.5 MPa. **(B)** Double row, p_s = 1.0 MPa. **(C)** Single row, p_s = 0.5 MPa. **(D)** Single row, p_s = 1.0 MPa.

Experiment

For the purpose of validating the mathematical model of the fluid in the journal cooler, the experiment was performed using one rotor test rig (illustrated in **Figure 7A**). In the test rig, a horizontal shaft rotation is automatically applied by an electro-spindle. The journal cooler is supported by a hub with a pressure transducers and a thermocouple. The cooling device is located in the middle of the cantilever of a rotor. The larger disc at the free end of cantilever is heated by electromagnetic induction at a restricted power of 1.6 kW. The cooler hub has a total of three radial threaded holes to supply the pressurized gas while allowing a transducers to be attached to gas in the annular cavity (**Figure 1**). The geometry of the tested cooler is presented in **Figure 1C**. With the Thermal imaging camera, temperature measurements of the shaft and the discs are examined in order to compare with the numerical results.

Figures 7B,C shows the measured and the predicted temperature distribution of the cantilever. The temperature image is captured when the rotor is thermally balanced, this is important for the comparison. The current pressure and temperature of the gas in the annular cavity are measured by the thermocouple and pressure sensor. These parameters will be used as boundary conditions for numerical calculation. The large disc on the right is used as the heat source, and the temperature value adopts the steady-state temperature measured in the experiment. The line *L1* in the figures is defined as temperatures of the cantilever in the direction of the center of the rotor, and its coordinate origin is on the left. The measured temperature on the horizontal line (*L1*) (see **Figure 7B**), is extracted on pixels. **Figure 7D** compares experimental and numerical temperatures on *L1*. These curves follow almost the same trend. It can be seen that both temperature curves (numerical and experimental) were subdivided into three main ranges. The range belonging to the shaft, is characterized by a small gradient, accompanied by small fluctuations (experiment results). This temperature is mainly determined by the cooling gas. The region belonging to the small disc is characterized by a significant increase in temperature gradient. The third region, located on the larger disc, remains roughly constant in temperature and can be considered a heat source. In this region, only a small gas flow is in contact with the surface.

As shown in the curves (**Figure 7D**), the numerical and measured temperature curve agree well. In the first region, slight deviation between CFD numeration and measurement

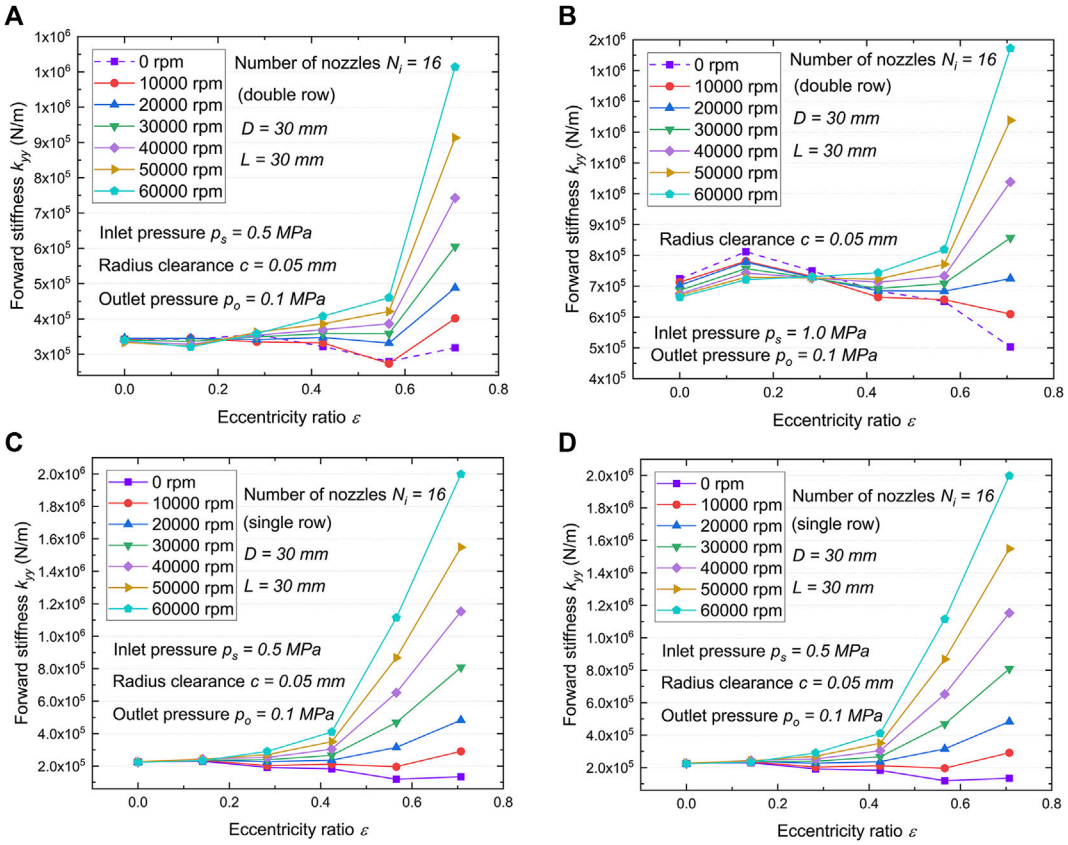

FIGURE 9 | Variations of forward stiffness coefficient k_{yy} with eccentricity ratio versus rotor speed. **(A)** Double row, p_s = 0.5 MPa. **(B)** Double row, p_s = 1.0 MPa. **(C)** Single row, p_s =0.5 MPa. **(D)** Single row, p_s =1.0 MPa.

exist. This might be traced back to shape difference and thermal resistance at the connection between the shaft and the disc which can cause uneven heat transfer. In addition, no temperature gradient of the large disc side surface are captured by the infrared thermal imaging camera.

Analysis of Dynamic Force Coefficients

This section discussed the force coefficient performance of cooling film versus eccentricity ratio and rotor speed for attitude angle of $\alpha = \pi/4$. Note that, the extreme large attitude angle is selected because the increase of journal attitude angle signifies the enhancement of the hydrodynamic instability effect caused by the cross-coupled force coefficient. The stiffness and damping characteristics analyses are conducted with the boundary conditions and geometric parameters in **Table 1**.

The variation tendency of the stiffness coefficient k_{xx} is relatively complicated. Hydrodynamic pressure caused by journal speed and static pressure from the nozzle have opposite effects on k_{xx}. The eccentricity (stiffness comes from static pressure) is the dominant factor at low journal speed and the opposite at high speed. The competition between the two forces causes the curves in the graphs to be distorted. In general, it first increases and then decreases with increasing journal eccentricity. The peak occurs between an eccentricity ratio equal to 0.14 and 0.283, depending on the cooling pressure and rotor speed.

Figures 8, **9** present the forward stiffness coefficient k_{xx} and k_{yy} versus eccentric ratio for varying journal speeds, respectively. As the rotor speed increases from 0 to 60,000 rpm, the k_{yy} (**Figure 9**) increases and k_{xx} decreases at higher speeds, demonstrating that journal speed can significantly change the pressure distribution in the radius clearance. In particular, the principal stiffness coefficient k_{xx} of the gas film is greatly reduced, for example, going from a maximum of 4.34×10^5 to a minimum of -1.04×10^5 N/m, when the journal eccentricity reaches 0.707 (**Figure 8D**). Negative principal stiffness (**Figure 8D**) can even occur at high rotational speeds and large eccentricity ratios, which is a potential threat to the system. Compared with the double row configuration, the minimum stiffness coefficients of k_{xx} and k_{yy} decrease for single row configuration (with a larger axial throttling distance) due to the decreased spacing between the nozzles over the circumference, but the maximum stiffness coefficients of k_{yy} (**Figure 9**) increase because of the raised rotational speed.

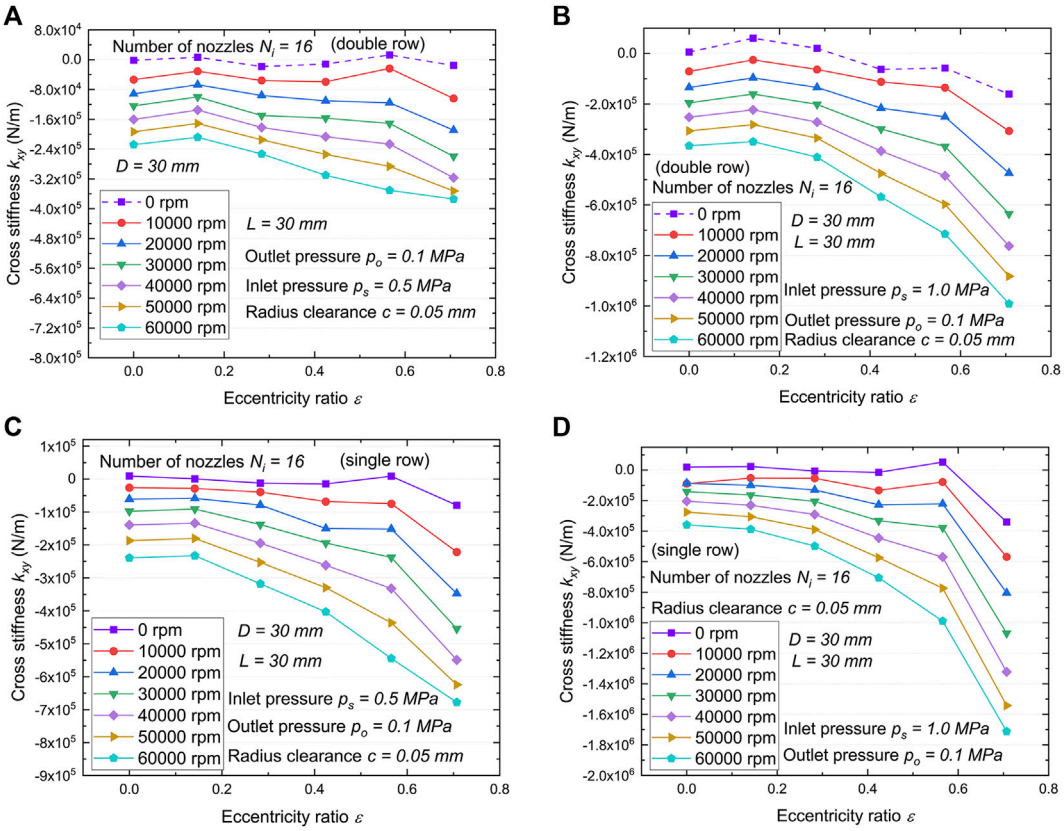

FIGURE 10 | Variations of cross stiffness coefficient k_{xy} with eccentricity ratio versus rotor speed. **(A)** Double row, p_s = 0.5 MPa. **(B)** Double row, p_s = 1.0 MPa. **(C)** Single row, p_s =0.5 MPa. **(D)** Single row, p_s =1.0 MPa.

A cooler model that does not consider hydrodynamic pressure effects will incorrectly estimate the force coefficient, due to the existence of unbalanced responses and misalignment of the rotor. **Figures 10**, **11** show the cross stiffness coefficient k_{xy} and k_{yx} versus eccentric ratio, respectively. In general, the cross stiffness coefficient increases with rotor speed and eccentric ratio while decreases with the number of nozzle rows. Cooler with the higher journal speed and stronger the gas film squeeze shows the larger k_{yy}, k_{xy} and k_{yx} (absolute value), and the single row with the more concentrated the hydrodynamic pressure effect (See **Figure 12**) demonstrates the larger the cross-coupling force coefficient.

Journal speed and eccentricity independent force coefficients are important because they contribute less indetermination to the prediction of dynamic response of turbine rotor systems. Moreover, cross-coupled terms with different signs and negative direct force coefficients in nearly all cases imply that the system is not stable or potentially destabilizing. The coupling of hydrodynamic effects may add energy to the rotor-bearing system, giving shaft rise to whirl in the direction of journal rotation, while the coupling of static pressure from the nozzle affects only the whirl orbit shape without enhancing the energy of the system. One of the purposes of the double-row and single-row nozzle configuration cases is to demonstrate the significance of hydrodynamic pressure effect in the gas film. The self-excitation effect at higher operating speeds is increased in view of the stiffening effect occurring in the CO2 film, which leads to increased reaction forces during rotor vibration in a squeezed region. In order to prevent promoting rotor whirl as hydrodynamic pressure effect was increased, it is necessary to select appropriate nozzle layout or take additional precautions.

The bump foil combined cooler can be considered to provide an additional compensation for journal eccentricity. As shown in the model in **Figure 13**, the cooler would then follow the eccentricity of the rotor by means of the deformation of the bump foil (See (Gad and Kaneko, 2016). for a full description on the computation of force coefficients for foil structures). Dry-friction between the bump foil and the cooler and between the bump foil and the housing inner surface provides energy dissipation damping well in excess of that obtained in the limited viscous friction of CO2. Yet the full potential of utilizing the foil's elastic deformation might be hindered by increasing asymmetry of the structural stiffness in the X- and Y-directions with increasing gas film force. Proper selection of the bump foil parameters is vital to exploiting the potential compensation for eccentricity. The ongoing research strives

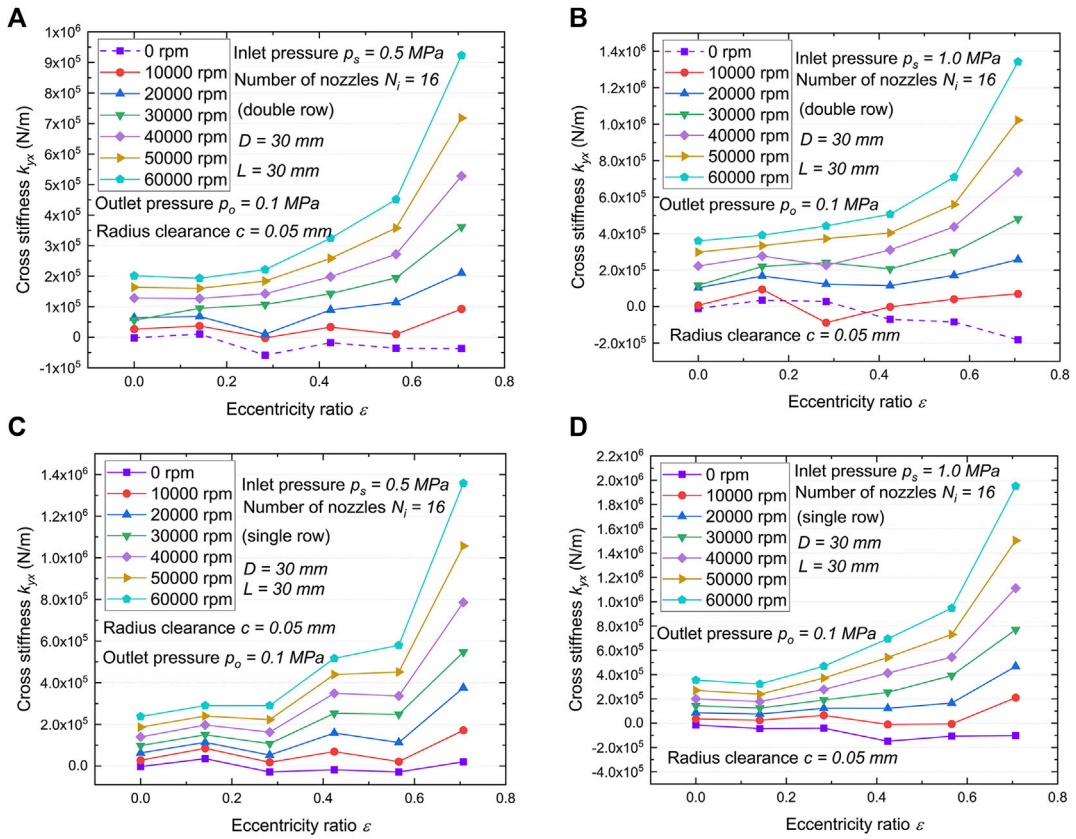

FIGURE 11 | Variations of cross stiffness coefficient k_{yx} with eccentricity ratio versus rotor speed. **(A)** Double row, p_s = 0.5 MPa. **(B)** Double row, p_s = 1.0 MPa. **(C)** Single row, p_s =0.5 MPa. **(D)** Single row, p_s =1.0 MPa.

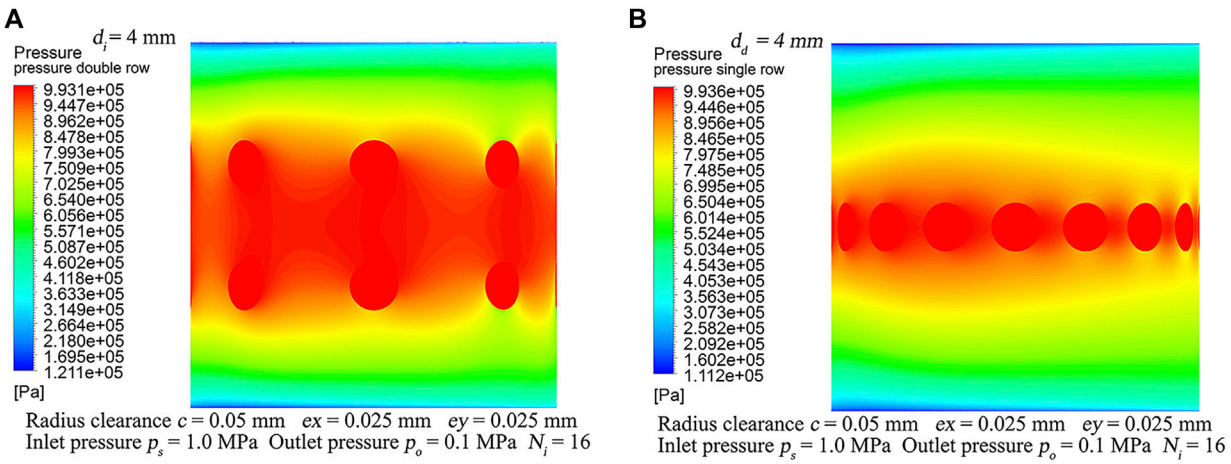

FIGURE 12 | Gas film hydrodynamic and static pressure coupling fields, e_x = 25 μm, e_y = 25 μm. **(A)** Double row. **(B)** Single row.

to address the eccentricity and frequency dependent properties of the force coefficient of cooler to eventually provide a cooling system that meets the temperature requirements of conventional bearings and dry gas seals in the SCO2 turbine rotor system at high-temperature and speed.

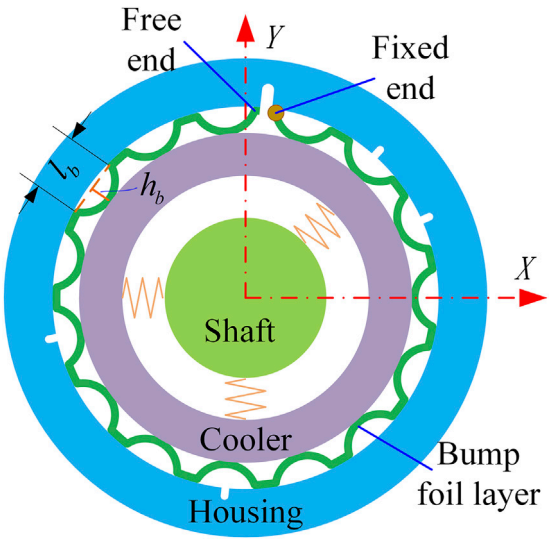

FIGURE 13 | Schematic view of typical cooler in bump-type.

CONCLUSION

The proposed air-film cooling device on the turboshaft is intended for application in a 300 kW SCO2 turbomachine to provide reliable thermal management while coping with the hydrodynamic pressure effects of the gas film. Dynamic force coefficients and heat transfer performance of the cooling device with a radius clearance of 50 microns are presented. Then, the present work investigated the comprehensive effect of nozzle arrangement and inlet pressure variation on the heat transfer performance of gas film. From the investigation, it can be concluded as follows:

1) CFD results shows a significant increase of cooling efficiency (also refers to mass flow utilization) with increase of the mass flow rate at a cooling pressure of less than 0.7 MPa, and then shows a gradual decay trend. Heat transfer capacity of the cooler are affected by nozzle arrangement at a given mass flow rate, that is, the temperature difference at the nozzle position directly determines the heat dissipation capacity. The fluid density and velocity in the radial clearance were selected as factors affecting heat transfer to be studied. Heat transfer performance is enhanced in terms of average Nusselt number by increasing average density in the radial clearance at a given inlet pressure. However, the correlation with the average velocity of the fluid in the clearance is not very manifest.
2) The average Nusselt number of the interface with double-row nozzle configuration is significantly higher than that of the single-row case. However, due to the asymmetry of the temperature distribution, the single-row arrangement has higher heat transfer efficiency for the turbine shaft. The cooling device with a single row nozzles operating at lower inlet pressures will have a higher mass flow utilization efficiency.
3) Gas film stiffness showed journal speed and eccentricity dependency, and the absolute value of the cross-coupling stiffness coefficient is higher at high frequencies and large eccentricity ratios. Cross-coupled terms generally have an explicit variation tendency than direct terms. The absolute value of results shows that the direct term have the opposite trend with eccentricity ratio, while the variation trend of the cross term with that is the same. In general, as the journal eccentricity ratio increases, the force coefficients, except for k_{xx}, increase accordingly. As the rotor speed increases, the absolute values of the cross stiffness and the direct stiffness k_{yy} increase, but the term of k_{xx} decreases.

DATA AVAILABILITY STATEMENT

The raw data supporting the conclusions of this article will be made available by the authors, without undue reservation.

AUTHOR CONTRIBUTIONS

JL mainly completes numerical simulation, experiment and paper writing HG and ZG provided the structural layout of the SCO turbine and the design of the cooling device. JsL directs the design and experiment of the testing machine. LL and YX completed the air film stiffness analysis.

FUNDING

This work is supported by the Special Project of Industrial Cluster in National Innovation Demonstration Zone (No. 201200210400) and the Program of Henan Center for Outstanding Overseas Scientists (No. GZS2018005).

ACKNOWLEDGMENTS

The authors would like to acknowledge the support from Henan Key Laboratory for Machinery Design and Transmission System. The authors wish to acknowledge also the turbine structure and guidance provided by the team of the University of Queensland, Australia.

REFERENCES

Adeoye, S., Parahovnik, A., and Peles, Y. (2021). A Micro Impinging Jet with Supercritical Carbon Dioxide. *Int. J. Heat Mass Transfer* 170, 14. doi:10.1016/j.ijheatmasstransfer.2021.121028

Afroz, F., and Sharif, M. a. R. (2020). Numerical Investigation of Heat Transfer from a Plane Surface Due to Turbulent Annular Swirling Jet Impingement. *Int. J. Therm. Sci.* 151. doi:10.1016/j.ijthermalsci.2019.106257

Ahmadi, M. H., Alhuyi Nazari, M., Ghasempour, R., Pourfayaz, F., Rahimzadeh, M., and Ming, T. (2018). A Review on Solar-assisted Gas Turbines. *Energy Sci Eng* 6 (6), 658–674. doi:10.1002/ese3.238

Ahmed, A., Wright, E., Abdel-Aziz, F., and Yan, Y. Y. (2021). Numerical Investigation of Heat Transfer and Flow Characteristics of a Double-wall Cooling Structure: Reverse Circular Jet Impingement. *Appl. Therm. Eng.* 189, 9. doi:10.1016/j.applthermaleng.2021.116720

Ahn, Y., Bae, S. J., Kim, M., Cho, S. K., Baik, S., Lee, J. I., et al. (2015). Review of Supercritical Co2 Power Cycle Technology and Current Status of Research and Development. *Nucl. Eng. Tech.* 47 (6), 647–661. doi:10.1016/j.net.2015.06.009

Alawadhi, K., Alfalah, A., Bader, B., Alhouli, Y., and Murad, A. (2021). An Optimization Study to Evaluate the Impact of the Supercritical CO2 Brayton Cycle's Components on its Overall Performance. *Appl. Sciences-Basel* 11 (5), 17. doi:10.3390/app11052389

Alotaibi, H. M., El Hassan, M., Assoum, H. H., Meraim, K. A., and Sakout, A. (2020). A Review Paper on Heat Transfer and Flow Dynamics in Subsonic Circular Jets Impinging on Rotating Disk. *Energ. Rep.* 6, 834–842. doi:10.1016/j.egyr.2020.11.124

Arslan, F., and Guzel, B. (2021). Numerical and Experimental Thermal-Hydraulic Performance Analysis of a Supercritical CO2 Brayton Cycle PCHE Recuperator. *Arabian J. Sci. Eng.* 14, 3. doi:10.1007/s13369-021-05464-3

Basumatary, K. K., Kumar, G., Kalita, K., and Kakoty, S. K. (2020). Stability Analysis of Rigid Rotors Supported by Gas Foil Bearings Coupled with Electromagnetic Actuators. *Proc. Inst. Mech. Eng. C: J. Mech. Eng. Sci.* 234 (2), 427–443. doi:10.1177/0954406219877903

Ehsan, M. M., Duniam, S., Li, J., Guan, Z., Gurgenci, H., and Klimenko, A. (2019). "A Comprehensive thermal Assessment of Dry Cooled Supercritical CO2 Power Cycles," in *Applied Thermal Engineering*. Langford Lane, Kidlington, Oxford, England: Pergamon-Elsevier Science Ltdthe Boulevard, 166. doi:10.1016/J.Applthermaleng.2019.114645

Feng, K., Li, W., Deng, Z., and Zhang, M. (2017). Thermohydrodynamic Analysis and Thermal Management of Spherical Spiral Groove Gas Bearings. *Tribology Trans.* 60 (4), 629–644. doi:10.1080/10402004.2016.1195467

Fp, I., Dp, D., and Tl, B. (2010). *Fundamentals of Heat and Mass Transfer*. New York, Inc: John Wiley & Sons.

Gad, A. M., and Kaneko, S. (2016). Tailoring of the Bearing Stiffness to Enhance the Performance of Gas-Lubricated Bump-type Foil Thrust Bearing. *Proc. Inst. Mech. Eng. J: J. Eng. Tribology* 230 (5), 541–560. doi:10.1177/1350650115606482

Han, D. J., Yang, J. F., Chen, C. T., and Tang, C. L. (2014). Experimental Research on the Dynamic Characteristics of Gas-Hybrid Bearing-Flexible Rotor System. *J. Vibroengineering* 16 (5), 2363–2374.

Ise, T., Imanishi, K., Asami, T., Tokumiya, T., Takada, N., Kimura, F., et al. (2014). Experimental Verification of Externally Pressurized Gas Journal Bearings with Asymmetric Gas Supply (Supply Gas Pressure Control Operation Using a Small Size Test Rig). *J. Adv. Mech. Des. Syst. Manufacturing* 8 (3), 11. doi:10.1299/jamdsm.2014jamdsm0029

Khatoon, S., Ishaque, S., and Kim, M. H. (2021). Modeling and Analysis of Air-Cooled Heat Exchanger Integrated with Supercritical Carbon Dioxide Recompression Brayton Cycle. *Energ. Convers. Manag.* 232, 16. doi:10.1016/j.enconman.2021.113895

Kim, S. H., Shin, H.-C., and Kim, S.-M. (2019). Numerical Study on Cooling Performance of Hybrid Micro-channel/micro-jet-impingement Heat Sink. *J. Mech. Sci. Technol.* 33 (7), 3555–3562. doi:10.1007/s12206-019-0649-7

Lapka, P., Cieplinski, A., and Rusowicz, A. (2020). Numerical Model and Analysis of Heat Transfer during Microjets Array Impingement. *Energy* 203, 9.

Lau, G. E., Mohammadpour, J., and Lee, A. (2021). Cooling Performance of an Impinging Synthetic Jet in a Microchannel with Nanofluids: An Eulerian Approach. *Appl. Therm. Eng.* 188, 19. doi:10.1016/j.applthermaleng.2021.116624

Lee, S., Yaganegi, G., Mee, D. J., Guan, Z. G., and Gurgenci, H. (2021). Part-load Performance Prediction Model for Supercritical CO2 Radial Inflow Turbines. *Energ. Convers. Manag.* 235, 11. doi:10.1016/j.enconman.2021.113964

Li, J., Gurgenci, H., Li, J. S., Li, L., Guan, Z. Q., and Yang, F. (2021). Optimal Design to Control Rotor Shaft Vibrations and thermal Management on a Supercritical CO2 Microturbine. *Mech. Industry* 22, 15. doi:10.1051/meca/2021023

Lubieniecki, M., Roemer, J., Martowicz, A., Wojciechowski, K., and Uhl, T. (2016). A Multi-Point Measurement Method for Thermal Characterization of Foil Bearings Using Customized Thermocouples. *J. Elec Materi* 45 (3), 1473–1477. doi:10.1007/s11664-015-4082-0

Maghrabie, H. M. (2021). Heat Transfer Intensification of Jet Impingement Using Exciting Jets - A Comprehensive Review. *Renew. Sust. Energ. Rev.* 139, 30. doi:10.1016/j.rser.2020.110684

Marchionni, M., Bianchi, G., and Tassou, S. A. (2021). Transient Analysis and Control of a Heat to Power Conversion Unit Based on a Simple Regenerative Supercritical CO2 Joule-Brayton Cycle. *Appl. Therm. Eng.* 183, 16. doi:10.1016/j.applthermaleng.2020.116214

Martowicz, A., Roemer, J., Lubieniecki, M., Zywica, G., and Baginski, P. (2020). Experimental and Numerical Study on the thermal Control Strategy for a Gas Foil Bearing Enhanced with Thermoelectric Modules. *Mech. Syst. Signal Process.* 138, 15. doi:10.1016/j.ymssp.2019.106581

Marzec, K. (2020). Influence of Jet Position on Local Heat Transfer Distribution under an Array of Impinging Nozzles with Non-planar Contour of the Cooled Surface. *Heat Transfer Eng.* 42, 1506–1521. doi:10.1080/01457632.2020.1800280

Menter, F. R. (1994). Influence of Free Stream Values on Turbulence Models for Engineering Applications. *AIAA J.* 30 (6), 1651–1659.

Modak, M., Sahu, S. K., and Park, H. S. (2021). An Experimental Study on Heat Transfer of Different Aqueous Surfactant Solutions Horizontal Impinging Jet Using Infrared Thermography. *Appl. Therm. Eng.* 188, 19. doi:10.1016/j.applthermaleng.2021.116668

Moore, J. J., Lerche, A., Allison, T., Ransom, D. L., and Lubell, D. (2011). Development of a High Speed Gas Bearing Test Rig to Measure Rotordynamic Force Coefficients. *J. Eng. Gas Turbines Power-Transactions Asme* 133 (10), 9. doi:10.1115/1.4002865

Pandey, V., Kumar, P., and Dutta, P. (2020). Thermo-hydraulic Analysis of Compact Heat Exchanger for a Simple Recuperated sCO(2) Brayton Cycle. *Renew. Sust. Energ. Rev.* 134, 21. doi:10.1016/j.rser.2020.110091

Patil, V. A., and Narayanan, V. (2005). Spatially Resolved Heat Transfer Rates in an Impinging Circular Microscale Jet. *Microscale thermophysical Eng.* 9 (2), 183–197. doi:10.1080/10893950590945058

Penkuhn, M., and Tsatsaronis, G. (2020). Systematic Evaluation of Efficiency Improvement Options for sCO(2) Brayton Cycles. *Energy* 210, 11. doi:10.1016/j.energy.2020.118476

Persico, G., Gaetani, P., Romei, A., Toni, L., Bellobuono, E. F., and Valente, R. (2021). Implications of Phase Change on the Aerodynamics of Centrifugal Compressors for Supercritical Carbon Dioxide Applications. *J. Eng. Gas Turbines Power-Transactions Asme* 143 (4), 11. doi:10.1115/1.4049924

Ryu, K. (2012). Prediction of Axial and Circumferential Flow Conditions in a High Temperature Foil Bearing with Axial Cooling Flow. *J. Eng. Gas Turbines Power-Transactions Asme* 134 (9), 6. doi:10.1115/1.4006841

San Andres, L., Ryu, K., and Kim, T. H. (2011a). Thermal Management and Rotordynamic Performance of a Hot Rotor-Gas Foil Bearings System-Part I: Measurements. *J. Eng. Gas Turbines Power-Transactions Asme* 133 (6). doi:10.1115/1.4001826

San Andres, L., Ryu, K., and Kim, T. H. (2011b). Thermal Management and Rotordynamic Performance of a Hot Rotor-Gas Foil Bearings System-Part II: Predictions versus Test Data. *J. Eng. Gas Turbines Power-Transactions Asme* 133 (6), 8. doi:10.1115/1.4001827

Siah Chehreh Ghadikolaei, S. (2021). Solar Photovoltaic Cells Performance Improvement by Cooling Technology: An Overall Review. *Int. J. Hydrogen Energ.* 46 (18), 10939–10972. doi:10.1016/j.ijhydene.2020.12.164

Tepe, A. Ü. (2021). Numerical Investigation of a Novel Jet Hole Design for Staggered Array Jet Impingement Cooling on a Semicircular Concave Surface. *Int. J. Therm. Sci.* 162. doi:10.1016/j.ijthermalsci.2020.106792

Tepea, A. Ü., Uysalb, Ü., Yetişkenc, Y., and Arslan, K. (2020). Jet Impingement Cooling on a Rib-Roughened Surface Using Extended Jet Holes. *Appl. Therm. Eng.* 178. doi:10.1016/j.applthermaleng.2020.115601

Turchi, C. S., Ma, Z. W., Neises, T. W., and Wagner, M. J. (2013). Thermodynamic Study of Advanced Supercritical Carbon Dioxide Power Cycles for Concentrating Solar Power Systems. *J. Solar Energ. Engineering-Transactions Asme* 135 (4), 7. doi:10.1115/1.4024030

White, M. T., Bianchi, G., Chai, L., Tassou, S. A., and Sayma, A. I. (2021). Review of Supercritical CO2 Technologies and Systems for Power Generation. *Appl. Therm. Eng.* 185, 28. doi:10.1016/j.applthermaleng.2020.116447

Zhang, B., Qi, S., Feng, S., Geng, H., Sun, Y., and Yu, L. (2018). An Experimental Investigation of a Microturbine Simulated Rotor Supported on Multileaf Gas Foil Bearings with Backing Bump Foils. *Proc. Inst. Mech. Eng. Part J: J. Eng. Tribology* 232 (9), 1169–1180. doi:10.1177/1350650117725463

Zhang, Y., Hei, D., Lü, Y., Wang, Q., and Müller, N. (2014). Bifurcation and Chaos Analysis of Nonlinear Rotor System with Axial-Grooved Gas-Lubricated Journal Bearing Support. *Chin. J. Mech. Eng.* 27 (2), 358–368. doi:10.3901/cjme.2014.02.358

Zywica, G., Baginski, P., and Bogulicz, M. (2021). Experimental and Numerical Evaluation of the Damping Properties of a Foil Bearing Structure Taking into Account the Static and Kinetic Dry Friction. *J. Braz. Soc. Mech. Sci. Eng.* 43 (1), 23. doi:10.1007/s40430-020-02720-9

Conflict of Interest: The authors declare that the research was conducted in the absence of any commercial or financial relationships that could be construed as a potential conflict of interest.

Publisher's Note: All claims expressed in this article are solely those of the authors and do not necessarily represent those of their affiliated organizations, or those of the publisher, the editors and the reviewers. Any product that may be evaluated in this article, or claim that may be made by its manufacturer, is not guaranteed or endorsed by the publisher.